1296 Vol. 8, No. 10 / November 2021 / Optica Research Article

OPTICA

Universal compressive tomography in the time-frequency domain

Jano Gil-Lopez,[1] Yong Siah Teo,[2,*] Syamsundar De,[1] Benjamin Brecht,[1] Hyunseok Jeong,[2] Christine Silberhorn,[1] and Luis L. Sánchez-Soto[3,4]

[1]Integrated Quantum Optics Group, Institute for Photonic Quantum Systems (PhoQS), Paderborn University, Warburger Straße 100, 33098 Paderborn, Germany
[2]Department of Physics and Astronomy, Seoul National University, 08826 Seoul, Republic of Korea
[3]Departamento de Óptica, Facultad de Física, Universidad Complutense, 28040 Madrid, Spain
[4]Max-Planck-Institut für die Physik des Lichts, Staudtstraße 2, 91058 Erlangen, Germany
*Corresponding author: ys_teo@snu.ac.kr

Received 12 April 2021; revised 24 August 2021; accepted 2 September 2021 (Doc. ID 427645); published 4 October 2021

Quantum state tomography is a basic tool in quantum information, but it becomes a challenging task that requires an immense number of measurement configurations as the system dimension grows. We implement an adaptive compressive tomography scheme capable of reconstructing any arbitrary low-rank spectral-temporal optical signal with extremely few measurement settings and without any ad hoc assumption about the initially unknown signal. This is carried out by implementing projections onto arbitrary user-specified optical modes. We present conclusive experimental results for both temporal modes and frequency bins, which showcase the versatility of our method and thereby introduce a universal optical reconstruction framework to these platforms.

https://doi.org/10.1364/OPTICA.427645

1. INTRODUCTION

Encoding quantum information in the time and frequency domains [1–3] has gained significant attention and has been proven to be a suitable alternative for scalable quantum information processing [4–6]. These encodings allow one to access high-dimensional Hilbert spaces, which may provide enhancements to quantum information extraction, cryptography, and communication tasks [7–13]. In addition, such encodings distinguish themselves by being directly compatable with single-mode fiber networks because they occupy only one single spatial mode. However, reliable time measurements with high sufficient resolution are still challenging, in particular at telecommunication wavelengths.

Achieving quantum performance in applications requires an efficient and trustworthy characterization of the experimental procedures, which is the scope of tomography. The proper and unambiguous estimation of quantum states with minimal resources is thus of paramount importance. The infinite-dimensional Hilbert space describing these encodings demands a computationally effective and experimentally feasible procedure.

Compressive schemes have been concocted to efficiently reduce the measurement settings required to reconstruct a signal [14]. However, they require a precise knowledge of the maximal rank of the unknown state, which is not always feasible in realistic scenarios. To bypass this drawback, in Refs. [15–19], new compressive schemes have been designed to characterize various low-rank states, gates, and measurements in different degrees of freedom. Crucially, they require no assumptions about the unknown quantum objects in question.

In this work, we develop and experimentally implement a compressive tomography in the time-frequency (TF) domain that allows us to uniquely determine unknown signal states that are near-coherent using very few measurement configurations. This is especially relevant in the single-photon regime [20–23], where a small number of copies of a state and practical limitations on measurement times require the efficient use of resources.

A critical component for our goal is the quantum pulse gate (QPG) [24–26], which can perform projections of a random input on tailored time-frequency modes. It is fed by spectrally shaped gating pulses to select time-frequency modes from the input. By shaping the gating pulse into all modes from a selected basis, one can fully scan a random input in the basis. We stress that the QPG operates on superpositions of time and/or spectral components. The QPG is already a well-stablished device for projective measurements on the temporal domain, and its complete tomography has been performed [27].

We shall first introduce the basic elements concerning the kinematic description of the electromagnetic field in the TF domain and the compressive state tomography applied to arbitrary near-coherent (low-rank) signal states encoded in this domain. After detailing the experimental techniques, we present a novel set of compressive tomography results for signals encoded in two broad classes of specral-temporal formats, namely, the temporal modes [27–29] that encode both temporal and spectral information and frequency bins [30–36] that reflect solely the spectral content. These results show that compressive characterization of arbitrary optical states is feasible and achievable with only a meager number of measurement settings.

2. PHOTON SPECTRAL-TEMPORAL MODES

A. Kinematics

In the following, we shall present the basic underlying formalism for our work, which applies to any spatially single-mode state of light. In general, we have to consider the photon-number degree of freedom when writing down the *complete* density operator of a (single spatial-mode) quantum state. To keep the manuscript clear and concise, we restrict all discussions to states that are well approximated in the single-photon subspace, with focus on their time-frequency modal properties. In this case, spectral-temporal modes can be considered as a complete basis set that represents all quantum states for a single photon (see [1]).

For a fixed polarization and transverse field distribution, a pure single-photon quantum state $\rho = |\psi\rangle\langle\psi|$ can hence be expressed as

$$|\psi\rangle = \int \mathrm{d}\omega a_\omega^\dagger |0\rangle \tilde{u}(\omega), \tag{1}$$

which is the coherent superposition of frequency modes, where $a_\omega^\dagger$ is the standard creation operator and $\tilde{u}(\omega)$ is the complex spectral amplitude of the wave packet. The ket $|\psi\rangle$ can alternatively be written as a superposition of temporal modes

$$|\psi\rangle = \int \mathrm{d}t a_t^\dagger |0\rangle u(t), \tag{2}$$

where the mode functions in the respective domains are Fourier transforms of each other. Such a state belongs to the infinite-dimensional Hilbert space spanned by the continuous bases $\{|t\rangle \equiv a_t^\dagger|0\rangle\}$ and $\{|\omega\rangle \equiv a_\omega^\dagger|0\rangle\}$. Both bases allow for a resolution of the identity

$$\int \mathrm{d}t|t\rangle\langle t| = \mathbb{1} = \int \mathrm{d}\omega|\omega\rangle\langle\omega|, \tag{3}$$

and their overlap is $\langle t|\omega\rangle = e^{it\omega}/\sqrt{2\pi}$, confirming that they are conjugate variables.

One can easily extend this formalism to describe mixed states in the form

$$\begin{aligned}\rho &= \int \mathrm{d}t' \int \mathrm{d}t'' |t'\rangle u(t', t'')\langle t''| \\ &= \int \mathrm{d}\omega' \int \mathrm{d}\omega'' |\omega'\rangle \tilde{u}(\omega', \omega'')\langle\omega''| \geq 0.\end{aligned} \tag{4}$$

Hermiticity imposes $u^*(t', t'') = u(t'', t')$ and $\tilde{u}^*(\omega', \omega'') = \tilde{u}(\omega'', \omega')$, whereas positivity gives

$$\int \mathrm{d}t u(t, t) = 1 = \int \mathrm{d}\omega \tilde{u}(\omega, \omega). \tag{5}$$

We mention that in spatial-temporal optics, ρ is also known as the coherence operator [37].

Since ρ encodes all information accessible in both domains, it is in principle possible to explore the full spectral-temporal content of a given signal by placing both time and frequency on equal footing. The most suitable way to do this is by using the so-called chronocyclic Wigner function [38–42], which is an adapted version of the original idea of Wigner [43]. It is defined as

$$\begin{aligned}W(t, \omega) &= 2 \int \mathrm{d}t' \mathrm{e}^{2i\omega t'} \langle t - t'|\rho|t + t'\rangle, \\ &= 2 \int \mathrm{d}\omega' e^{-2i\omega' t} \langle\omega - \omega'|\rho|\omega + \omega'\rangle,\end{aligned} \tag{6}$$

with normalization $\int \mathrm{d}t'\mathrm{d}\omega' W(t', \omega')/(2\pi) = 1$. The term "chronocyclic" signifies the juxtaposed appearances of both time and frequency variables.

A practical TF encoding can be accomplished through basis projections [44]. More specifically, by employing a finite set of states $\sum_{n=0}^{d-1} |\phi_n\rangle\langle\phi_n| = \mathbb{1}_d$ that span a d-dimensional subspace, we may define the d-dimensional state

$$\rho_d = \sum_{n,n'=0}^{d-1} |\phi_n\rangle\langle\phi_n|\rho|\phi_{n'}\rangle\langle\phi_{n'}|. \tag{7}$$

A handy basis to express this finite-dimensional state is the set of Hermite–Gaussian (HG) modes [45–48] ($|\phi_n\rangle \equiv |\mathrm{HG}_n\rangle$)

$$\langle t|\mathrm{HG}_n\rangle = \frac{1}{\sqrt{\pi^{1/2} 2^n n!}} e^{-t^2/2} H_n(t), \tag{8}$$

where $H_n(\cdot)$ is the Hermite polynomial. In these modes, the Wigner function takes the form [49,50]

$$\begin{aligned}W(t, \omega) = 2e^{-2|\alpha|^2} &\sum_{n,n'=0}^{d-1} (-1)^{n_<} \rho_{nn'} \frac{2^{n_>}}{2^{n_<}} \sqrt{\frac{n_<!}{n_>!}} \\ &\times |\alpha|^{n_> - n_<} e^{-i(m-n)\theta} L_{n_> - n_<}^{(n_<)} \left(4|\alpha|^2\right),\end{aligned} \tag{9}$$

where $\rho_{nn'}$ are the matrix elements of ρ in that basis, $L_n^{(\mu)}(\cdot)$ is the associated Laguerre polynomial, $\alpha = (t + i\omega)/\sqrt{2} = |\alpha|e^{i\theta}$, $n_> = \max\{n, n'\}$, and $n_< = \min\{n, n'\}$. For the HG modes, the Wigner function reduces to

$$W_n(t, \omega) = 2(-1)^n e^{-(t^2+\omega^2)^2} L_n\left(2t^2 + 2\omega^2\right), \tag{10}$$

that is, simple Laguerre–Gaussian functions.

Pulse shapers [51] can be used to generate temporal modes of arbitrary spectral-temporal content. As a special case, one can fashion pulses that are well enveloped only in the frequency domain. A specific type of such pulses are frequency bins, where discrete spectra of narrowband frequencies are selected to define their single-mode states. From the spectral decomposition in Eq. (4), the mode amplitude $\tilde{u}(\omega', \omega'')$ of these frequency bins takes the ideal form

$$\tilde{u}(\omega', \omega'') = \sum_{n,n'=0}^{d-1} \tilde{u}_{nn'} \delta(\omega' - \omega_n)\delta(\omega'' - \omega_{n'}), \tag{11}$$

for a set of d frequency bands $\{\omega_n\}_{n=0}^{d-1}$. It proves often convenient to consider equally spaced frequencies $\omega_n = \omega_0 + \Delta\omega[n - (d-1)/2]$ about a central frequency ω_0 with a level spacing of $\Delta\omega$. The resulting d-dimensional frequency-bin state derived from the second equality in Eq. (4),

$$\rho = \sum_{n,n'=0}^{d-1} |\omega_n\rangle \tilde{u}_{nn'} \langle \omega_{n'}|, \tag{12}$$

thus has the Wigner function

$$W(t, \omega) = \sum_{n,n'=0}^{d-1} \tilde{u}_{nn'} e^{i(\omega_n - \omega_{n'})t} \delta(\omega - (\omega_n + \omega_{n'})/2). \tag{13}$$

Although $W(t, \omega)$ is now plane-wave oscillatory in t and singular in ω, as is expected from an overidealized model that has perfectly well-defined frequency bands of zero width in the spectral domain, terms in t and ω may be disregarded, as they are auxiliary. Operationally, it is the complex amplitudes $\tilde{u}_{nn'}$ that truly contain all purely spectral information about the frequency-binned system and can hence be easily represented by their positive matrix $\tilde{\boldsymbol{u}} = \sum_{n,n'=0}^{d-1} \boldsymbol{e}_n \tilde{u}_{nn'} \boldsymbol{e}_{n'}{}^T$ in some computational basis $\{\boldsymbol{e}_n\}$.

B. Generalized Measurements with the Quantum Pulse Gate

An ideal QPG mode matched to the source acts on an arbitrary single-photon input state ρ_{in} according to [1]

$$\rho_{\text{out}} = Q_\theta^\zeta \rho_{\text{in}} Q_\theta^{\zeta\dagger}, \tag{14}$$

where

$$Q_\theta^\zeta = \mathbb{1} - |A^\zeta\rangle\langle A^\zeta| - |B\rangle\langle B| + \cos\theta\left(|A^\zeta\rangle\langle A^\zeta| + |B\rangle\langle B|\right) + \sin\theta\left(|B\rangle\langle A^\zeta| - |A^\zeta\rangle\langle B|\right), \tag{15}$$

and

$$|A^\zeta\rangle = A^{\zeta\dagger}|0\rangle \equiv \int \mathrm{d}\omega a_\omega^\dagger |0\rangle \zeta(\omega) \tag{16}$$

is the source mode. This consists of a family of unitary transformations on the single-photon state space composed of two nonoverlapping frequency bands: one spanned by the input mode state $|A^\zeta\rangle$ and a single TF mode $|B\rangle$ occupying the other. Note that this operation describes a special quantum mechanical beam splitter as sketched in Fig. 1.

Given an input state with photon mean number N_ρ, the mean photon number in the output mode $|B\rangle$ of the QPG is

$$\langle N_\rho^\zeta \rangle = N_\rho \eta |\gamma_\rho^\zeta|^2, \tag{17}$$

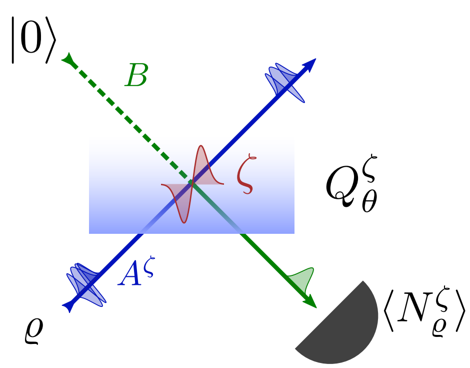

Fig. 1. QPG implements a beam splitter operation between two sets of modes $\{A\}$ and $\{B\}$, where one user-chosen input mode A^ζ is converted to an output mode B, while all other modes are transmitted. Photon detection in the output mode then implements a projection of an input state ρ onto mode A^ζ.

with $\eta = \sin^2\theta$ the conversion efficiency of the QPG and $\gamma_\rho^\zeta = \langle A^\zeta|\rho|A^\zeta\rangle$ the overlap between the input mode $|A^\zeta\rangle$ of the QPG and the input state ρ.

Only the part of ρ overlapping with the QPG input mode is converted to mode $|B\rangle$. Subsequent photon counting in this mode then effectively implements a projection of ρ onto $|A^\zeta\rangle$, where $|A^\zeta\rangle\langle A^\zeta|$ is a projector of a measurement basis.

3. RANDOMIZED COMPRESSIVE TOMOGRAPHY

A rank-r state of dimension d, described by a positive unit-trace operator ρ_d, can be uniquely determined by $(2d - r)r - 1$ independent parameters. On the other hand, a set of $\lceil[(2d - r)r - 1]/(d - 1)\rceil$ measurement bases generally cannot fully characterize such a state (here, $\lceil \times \rceil$ denotes the ceiling function giving the least integer greater than or equal to x). For instance, it has been shown that two bases can never fully characterize arbitrary states of $d = 2$—the finite version of the Pauli problem [52,53]. Nevertheless, one can still search for a set of $M \ll O(d^2)$ measurement outcomes that can unambiguously reconstruct the set of states of known rank $r \ll d$. We call such a measurement set informationally complete (IC). However, when r and all other information about ρ are unknown to the observer, surmising that a fixed set of measurements with an $M \ll O(d^2)$ would completely determine ρ_d before a tomography experiment generally leads to unreliable reconstruction results.

In this section, we introduce a randomized compressive tomography scheme (RCT) for characterizing an unknown low-rank time-frequency state ρ_d of a finite dimension d and rank $r \ll d$. We show that, without resorting to any ad hoc assumption about ρ_d, we can still determine whether a given number $M \ll O(d^2)$ of randomly chosen orthonormal bases can uniquely reconstruct ρ_d. Each basis is denoted as $\mathcal{B}_k = \{|b_{k0}\rangle, |b_{k1}\rangle, \ldots, |b_{kd-1}\rangle\}$, with $\sum_{l=0}^{d-1} |b_{kl}\rangle\langle b_{kl}| = \mathbb{1}$. This scheme is therefore universal, in the sense that with it, states of arbitrary time-frequency modes can be compressively characterized using general bases measurements that can be very reliably generated using the QPG as discussed in Section 2.B.

The RCT scheme is a bottom-up iterative procedure, in which independent bases $\mathcal{B}^{(k)} = \{\mathcal{B}_1, \mathcal{B}_2, \ldots, \mathcal{B}_k\}$ are chosen and measurements in these bases are made on independent and identically prepared copies of the state. The resulting outcomes and data are accumulated until the time-frequency state estimator $\hat{\rho}_d \geq 0$ is unique. When this happens, it implies that apart from $\hat{\rho}_d$, there is no other state that is consistent with the measurements. More specifically, in the kth iterative step, after a basis $\mathcal{B}_k$ is measured, the accumulated bases set $\mathcal{B}^{(k)}$ and corresponding relative frequency data $\boldsymbol{\nu}_k = (\nu_{10}, \nu_{11}, \ldots, \nu_{1d-1}, \ldots, \nu_{k0}, \nu_{k1}, \ldots, \nu_{kd-1})^\top$ for these bases ($\sum_{l=0}^{d-1} \nu_{kl} = 1$) are analyzed to see if these measurements are IC.

This procedure involves two following stages as illustrated in Fig. 2. In the first stage, the column of raw relative frequencies $\boldsymbol{\nu}_k$ are mapped to the corresponding column $\hat{\boldsymbol{p}}_k$ whose elements $\hat{p}_{kl} = \langle b_{kl}|\rho_d|b_{kl}\rangle$ are physical probabilities obtained from some positive unit-trace operator ρ_d. This mapping is necessary to ensure that the analysis is physical. For this, we may invoke the maximum-likelihood (ML) method [54–58] that would give us the column $\hat{\boldsymbol{p}}_k$ that maximizes the likelihood function describing the QPG measurement scenario over the physical d-dimensional state space [59].

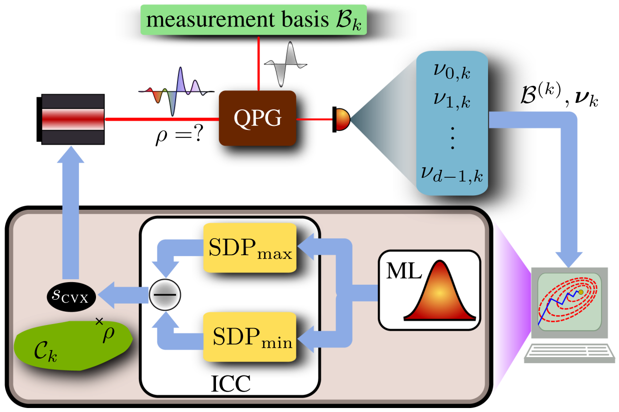

Fig. 2. Schematic figure of the iterative RCT scheme. The signal carrying the unknown state ρ interacts with the QPG so that a randomly chosen basis is measured in the kth step. This gives a set of relative frequencies that is combined with previous measurements. All k measured bases $\mathcal{B}^{(k)}$ and their corresponding relative frequencies $\boldsymbol{\nu}_k$ are then processed numerically by first carrying out the ML routine to obtain physical probabilities, and next subjecting the results to the ICC algorithm that computes the completeness indicator s_{CVX} using two semidefinite programs (SDPs) (discussed in Appendix A). The whole cycle repeats until s_{CVX} drops below a certain small threshold at $k = K_{\mathrm{IC}}$, implying that $(\mathcal{B}^{(K_{\mathrm{IC}})}, \boldsymbol{\nu}_{K_{\mathrm{IC}}})$ is IC.

The second stage of RCT at the kth step is to find out if there is more than one state that gives such physical ML probabilities p_{jk}—the informational completeness certification (ICC). If this were true, then in principle there will be convex set ($\mathcal{C}_k$) of states with a nonzero volume. The task is to deterministically figure out the value $k = K_{\mathrm{IC}}$ at which the volume of $\mathcal{C}_{K_{\mathrm{IC}}}$ is zero. To do this, we introduce an indicator s_{CVX} that monotonically decreases with the convex-set volume. When $s_{\mathrm{CVX},K_{\mathrm{IC}}} = 0$, it can be argued easily that $\mathcal{C}_{K_{\mathrm{IC}}}$ is a single point, telling us that $[\mathcal{B}^{(K_{\mathrm{IC}})}, \boldsymbol{\nu}_{K_{\mathrm{IC}}}]$ is IC [15]. The computation of s_{CVX} can be done with the help of semidefinite programming and is explained in Appendix A.

In TF optical experiments, the state $\rho = \rho_d$ (or the coherence operator) encodes all information about the spectral-temporal content of the source. The bases data $\boldsymbol{\nu}_k$ are a collection of normalized count rates that is proportional to the intensity expectation value. The relevant measurement bases are designed with the QPG and additional optical components that manipulate signals in the TF domain. Since the state ρ_d essentially is endowed with all the properties of a quantum state, we may directly apply the RCT scheme to compressively reconstruct any unknown rank-deficient ρ in such settings.

4. EXPERIMENTAL TECHNIQUES

In our realization, we implement the QPG with a group-velocity-matched (GVM) sum-frequency generation in a periodically poled, 35 mm long, and 7 µm wide titanium in-diffused lithium niobate waveguide. The 4.4 µm poling period grants quasi-phase-matching at the desired GVM wavelengths; 1541 nm for the input state ρ and 857 nm for the pump mode ζ. The GVM process is engineered so that the output mode $|B\rangle$ at 554 nm is solely defined by the phase-matching function $\phi(\omega_{\mathrm{in}}, \omega_{\mathrm{out}})$ of the process. This realizes the mode-selective process described in Section 2.B.

The transfer function is then the product of the phase-matching function and the pump mode envelope $\varphi(\omega_{\mathrm{in}}, \omega_{\mathrm{out}}) = \zeta(\omega_{\mathrm{pump}})\phi(\omega_{\mathrm{in}}, \omega_{\mathrm{out}})$. It describes the relation between input and output frequencies for the SFG process. An example of a transfer function with a first-order Hermite–Gaussian envelope of the pump mode is depicted in the inset in Fig. 3(b). Only the parts of the input state that overlap with the transfer function will be converted to the output and detected with a single-photon detector. Hence, for any input state, the QPG performs a projective measurement on the mode defined by the pump.

In its current realization, the QPG provides one single output only. In consequence, we must sequentially project onto the basis components for the RCT measurement. This is, however, not a limitation, since RCT requires only information about the mean occupation per measurement mode and no intermodal correlations. The concept of the QPG readily generalizes to implementations that provide multiple parallel outputs and hence facilitate the simultaneous measurement of several basis components [60], which reduces overall measurement times but does not lead to an improved overall performance of RCT.

Signal and pump fields are emitted from a titanium-sapphire (Ti:Sa) laser and an optical parametric oscillator (OPO) with a repetition rate of 80 MHz. These coherent-state fields are then attenuated to the few-photon level, and we have demonstrated in earlier work that the quantum pulse gate does not change the photon-number statistics of the incoming signal light. We emphasize that one may safely assume that the photon statistics of the signal are Poissonian, such that the terminology "quantum state tomography" is still appropriate.

The few-photon signal is shaped into the appropriate input time-frequency states ρ_{in} using a fiber-coupled commercial spectral shaper (Finisar Waveshaper). The output of the shaper is then coupled to the QPG in free space with a lens. A delay line is used to match the arrival time of the signal pulses to those of the pump at the QPG. The pump field is sent to a home-built spectral shaper setup consisting of a holographic grating (2000 lines/mm), a cylindrical mirror, and a spatial light modulator (SLM) (Hamamatsu LCOS-SLM X12513-07) in a folded $4f$ line configuration. This allows us to shape the pump envelope ζ into any base component for the RCT measurements. The shaped pump pulses are then coupled to the QPG through the same optical path as the input field.

At the output of the QPG, the unconverted input and transmitted pump fields are separated from the upconverted output with dichroic mirrors. The upconverted green output field is then sent to a tunable spectral filter consisting of a grating, a lens, and a slit with a variable width with a mirror on its back, in a folded $4f$ line configuration. The filter is set to 30 pm FWHM to filter out the sidelobes of the QPG sinc phase-matching function [51] and to further increase the selectivity of the mode-selective process. The filtered output is then sent to an avalanche photon detector (APD) (ID Quantique) connected to a time-tagger (Swabian Instruments) to collect the measurement data.

We calculate the number of photons per input pulse from the measured output counts in the APD from test measurements that were conducted between measuring different bases. In these measurements, the pump was set to fully overlap with the input signal, which allowed us to track drifts during the duration of a measurement. The total output APD counts during one 20 ms duration measurement are

$$C_{\mathrm{output}} = \eta N_{\mathrm{input}}, \tag{18}$$

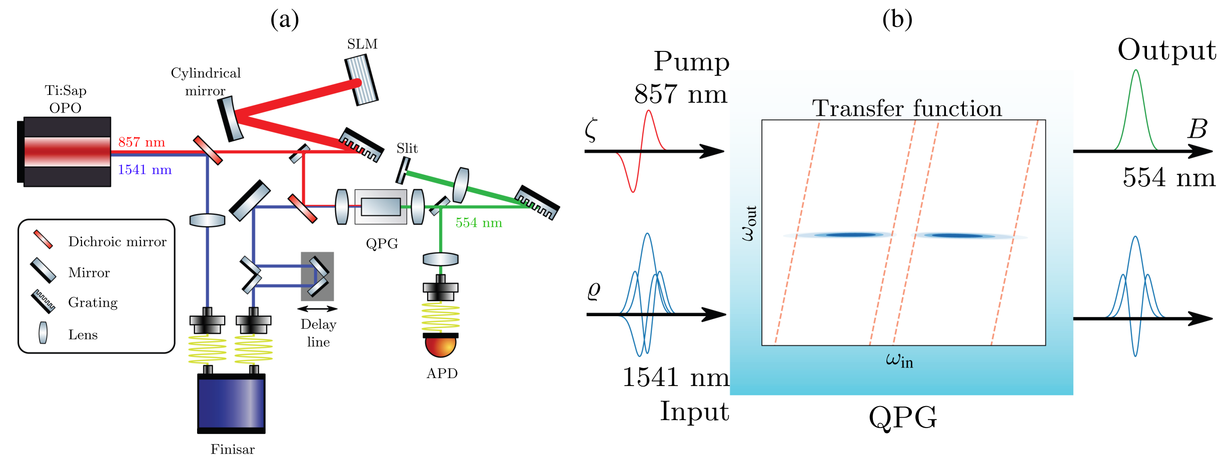

Fig. 3. (a) Experimental setup. A Ti:Sa-OPO laser system emits ultrafast pulses at the required wavelengths. The input signal at telecommunication wavelengths is spectrally shaped using a commercial shaper, and the pump field is shaped using a home-built $4f$ line shaper setup with an SLM device. A delay line on the input field arm is used to match it temporally with the pump field for the QPG process. At the output of the QPG, unconverted input and throughput pump are separated from the output field with dichroic mirrors that were not depicted to simplify the sketch. The output field is then filtered with a homemade spectral filter and sent to the APD. (b) Experimental realization of the QPG. Input and pump fields are coupled into the QPG waveguide device where the process's transfer function selects the mode A^{ζ} from the input state ρ and upconverts it to the output mode B. The transfer function $\varphi(\omega_{\rm in}, \omega_{\rm out})$ inside the QPG describes the relation betwen the input and output frequencies depending on the phase-matching function ϕ and the pump mode ζ. The pump amplitude at $1/e^2$ is plotted in red dashed lines as a reference.

where $N_{\rm input}$ is the total number of input photons and $\eta = \eta_{\rm APD}\, \eta_{\rm fiber}\, \eta_{4f}\, \eta_{\rm QPG}$ comprises the efficiencies of the APD $\eta_{\rm APD} = 50\%$, the fiber coupling to the APD $\eta_{\rm fiber} = 50\%$, the total $4f$ line setup transmission $\eta_{4f} = 10\%$, and the QPG conversion efficiency $\eta_{\rm QPG} = 3\%$. The latter is due to low pulse energies of the shaped pump pulses, and we note that this is not a fundamental limit as reviewed by some of the authors in [61]. From 14×10^3 counts in the output in the 1.52×10^6 pulses of the 20 ms duration single measurement, the number of photons per pulse in the input field is ≈ 12. This number was chosen as compromise between photon-level input light and total measurement time; the QPG has already been used for the conventional time-frequency tomography of genuine heralded single photons [47].

The input states to be reconstructed are chosen to be either temporal modes whose envelopes are HG functions or frequency bins of dimension d. The temporal modes have an spectral FWHM of 1 THz, and the frequency bins are 0.07 THz wide. The pump modes are then shaped into the d-dimensional randomly rotated basis modes $\mathcal{B}_k$ of each input state. Note that RCT exhibits compressive effects with any pump modes, since the ICC procedure always decisively verifies whether any given measurement dataset is IC regardless of the unknown state.

The rotation uses randomly generated unitary matrices. This necessarily means that the overlap between each single measurement mode and the signal may be low, since we do not assume any prior knowledge about the signal. While this leads to low overall count rates per measurement mode, this is not an issue here; the QPG does not add noise to the converted output signal [47]. Given that the detector has sufficiently low dark counts, a low spectral overlap between the signal and measurement mode will not reduce the RCT performance. Furthermore, a longer measurement time can help to increase the total count rates per measurement mode. In general, this is a challenge every quantum state tomography has to overcome in one way or another.

We generate between 100 and 200 bases of M randomly rotated bases modes, M being equal to the dimension d chosen for the experiment. The projection onto each mode of each base is measured for 20 ms on the APD. The resulting raw counts $\langle N^{\zeta}_{\rho} \rangle$ at the output B are measured and stored. The experimental procedure and the raw counts from the measurements of a complete ten-dimensional basis are showcased in Fig. 5. The relative frequencies ν_{jk} are then calculated from the raw counts with the repetition rate of the laser and the measurement time. Every 10 measurements, the time delay between signal input and pump is realigned automatically by maximizing the mode selectivity to account for drifts in the setup. To realize measurements on mixed input states, we measure different inputs with the same set of randomly rotated bases. We then mix the measured data with appropriate weights in postprocessing.

The randomly rotated bases implement a nonuniform sampling of the input state that accomplishes compressive sensing [62,63]. In a sense, the QPG can be considered a single-pixel camera for temporal modes. States with temporal features much faster than the resolution of the single-photon detector are reconstructed by modulating the input signal with random temporal masks. In addition, the use of compressed sensing facilitates signal reconstruction with fewer measurements than a direct sampling approach [64]. This is especially beneficial in situations in which a signal must be reconstructed from a limited number of photons.

5. RESULTS

A. Temporal Modes

The first class of low-rank TF states we shall use to demonstrate the RCT scheme constitutes the HG modes and their statistical mixtures. These are highly relevant, as they closely approximate the eigenbasis of parametric downconversion processes [65] and have been shown to be optimal for certain metrology tasks. In terms of their chronocyclic Wigner function representation, states corresponding to the first three HG modes, for instance, are expressed as

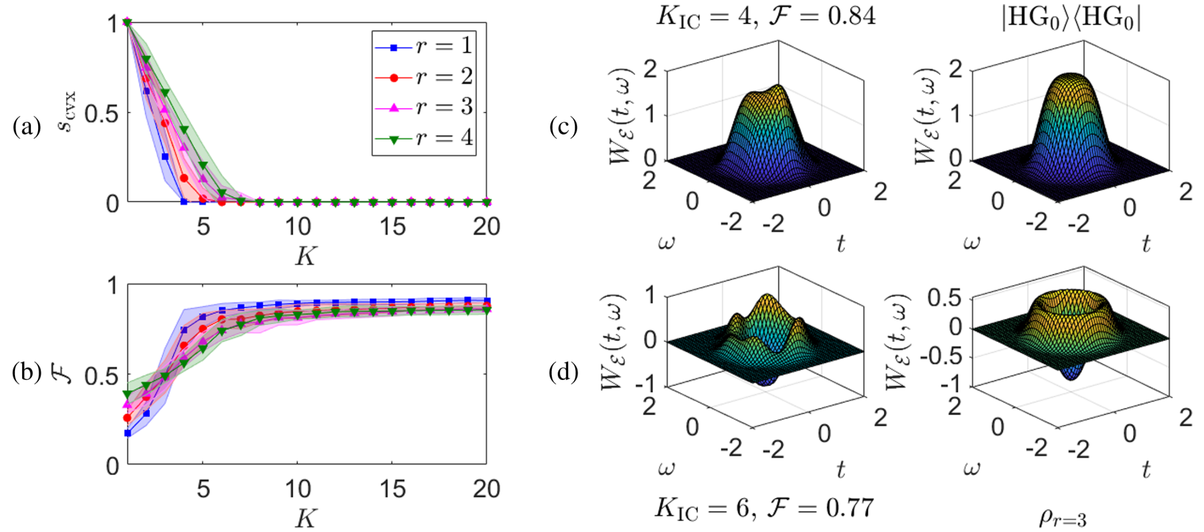

Fig. 4. Reconstruction results for time-frequency states of $d=10$ with respect to the number of bases measured (K). (a) and (b) The average drop in s_{CVX} for each state rank r coincides with the average rise in fidelity $\mathcal{F}$. The 1-σ error regions are computed with 10 experimental runs per value of r. For $r>1$, each run is conducted with a state that is a randomized mixture of the components $\{|\mathrm{HG}_0\rangle\langle\mathrm{HG}_0|,\ldots,|\mathrm{HG}_{r-1}\rangle\langle\mathrm{HG}_{r-1}|\}$. The value of K_{IC} for which $s_{\mathrm{CVX},K_{\mathrm{IC}}}=0$ steadily increases with r as it should. Whenever $s_{\mathrm{CVX}}\neq 0$, $\mathcal{F}$ is computed for $\rho_{\min}$ (see Appendix A). (c) and (d) Sample Wigner functions for the rank-one HG_0 mode and a random rank-three mixture of the HG modes ($\rho_{r=3}=|\mathrm{HG}_0\rangle 0.17\langle\mathrm{HG}_0|+|\mathrm{HG}_1\rangle 0.70\langle\mathrm{HG}_1|+|\mathrm{HG}_2\rangle 0.13\langle\mathrm{HG}_2|$) are shown.

$$W_{n=0}(t,\omega)=2e^{-y^2},$$

$$W_{n=1}(t,\omega)=2e^{-y^2}(2y-1),$$

$$W_{n=2}(t,\omega)=2e^{-y^2}(2y^2-4y+1), \tag{19}$$

where $y=t^2+\omega^2$. These states are all rotationally symmetric in the spectral-temporal content.

A total of ten HG basis modes, $\sum_{n=0}^{9}|\mathrm{HG}_n\rangle\langle\mathrm{HG}_n|=\mathbb{1}_{10}$, are used to project ρ onto a finite-dimensional subspace of dimension $d=10$. Random von Neumann basis measurements of the same dimension are generated with the QPG to collect measurement data for the rank-one modes HG_0, HG_1, HG_2, and HG_3, and their statistical mixtures. These basis measurements are parametrized by random unitary rotations distributed according to the Haar measure [66]. Figure 4 shows the results for the different low-rank time-frequency states. For the rank-one graphs in panels (a) and (b), the results are averaged over experimental runs of all the four HG modes.

As the number of independent parameters characterizing a rank-r state increases roughly linearly in r for $r\ll d$, the number of measurement bases needed to uniquely reconstruct rank-r states should also increase linearly in r in this regime [16].

To gain further insights into this point, in Fig. 6 we present all important simulation plots that showcase the average scaling behavior (over 20 random rank-r states distributed uniformly with respect to the Hilbert–Schmidt measure [67]) of K_{IC} in the absence of statistical fluctuation. After simulating quantum systems of various dimensions, numerical evidence clearly shows that K_{IC} is linear in both r and $\log d$. While the precise fitted expression is given in the figure caption within the 95% confidence level, we state the underlying ansatz form $K_{\mathrm{IC}}=(\alpha r+\beta)(\log d+a\log r)-ar+b$ that is used to compare with the experimental values. For $d=10$, we have the theoretical predictions $K_{\mathrm{IC}}=3.92$, 6.08, and 7.60 for the ranks $r=1$, 2, and 3, respectively. This characteristic behavior can be already observed in Figs. 4(a) and 4(b), despite the presence of statistical noise and experimental imperfections in the measurement data. Note also that K_{IC} may be very different from the results considered in conventional compressed-sensing protocols, which heavily rely on the rank assumption *without* ICC.

The choice of an effective dimension d to describe an optical state depends on the actual context, and various calibration techniques can be used to estimate this dimension. For our purpose, since the tested HG projectors span a four-dimensional subspace, it is clear that $d=10$ is sufficient to describe any statistical mixture of these projectors. In Fig. 7 we give the plots of s_{CVX} and fidelity $\mathcal{F}$ for the $|\mathrm{HG}_0\rangle\langle\mathrm{HG}_0|$ projector in dimensions $d=10$, 20, 40, and 60, all derived from real experimental data. The results confirm, as they should, that larger dimensions evidently do not affect the results of RCT so long as these Hilbert spaces adequately contain all physical features of the unknown state, which is clearly the case for this projector.

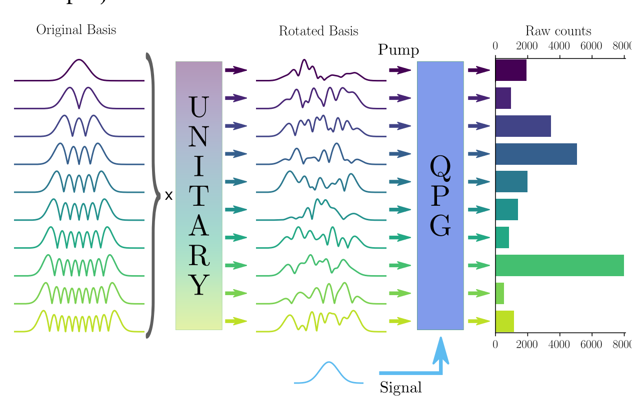

Fig. 5. Experimental measurements for a ten-dimensional basis. The original HG modes are rotated through a unitary to form a new basis. Each mode of the rotated basis is then sent as a pump to the QPG with a the signal under investigation, and the converted raw counts are measured. The raw counts are then used to obtain the relative frequencies and perform one loop of the RCT.

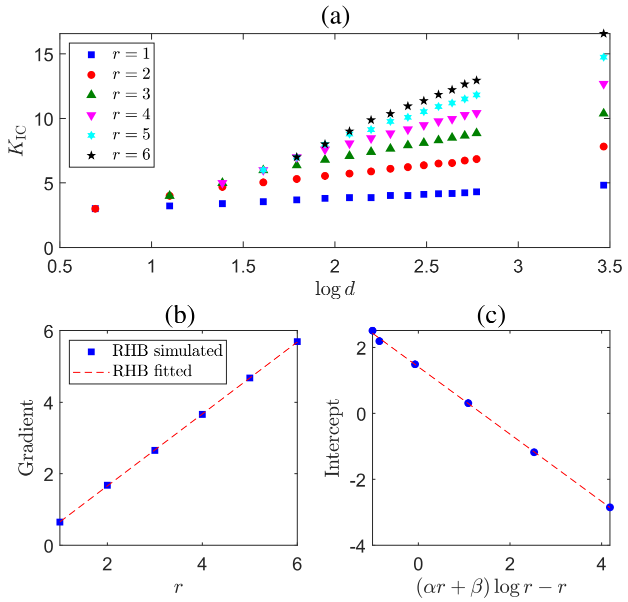

Fig. 6. Graphical summary of revealing the compressivity for random Haar bases (RHB). (a) The scaling behavior for $K_{\rm IC}=m_r\log d+c_r$ is linear in $\log d$ for all simulated dimensions $d\in\{2,3,\ldots,16,32\}$. For the tested ranks $1\leq r\leq 6$, (b) the gradient turns out to be $m_r=\alpha r+\beta$ with $\alpha=1.006\pm0.009$ and $\beta=-0.3528\pm0.0359$, and (c) the intercept $c_r=a[(\alpha r+\beta)\log r-r]+b$ involves $a=-1.02\pm0.03$ and $b=1.407\pm0.075$. All error intervals are of 95% confidence.

B. Frequency Bins

The second class of low-rank states that we consider here are frequency-bin states. These are states defined by a discrete set of narrowband frequency bins. The corresponding complex matrix $\tilde{u}$ that dresses these continuous frequency bases inasmuch as Eq. (11) is a positive matrix that contains the full information about a general state defined by these frequency bins in the spectral domain.

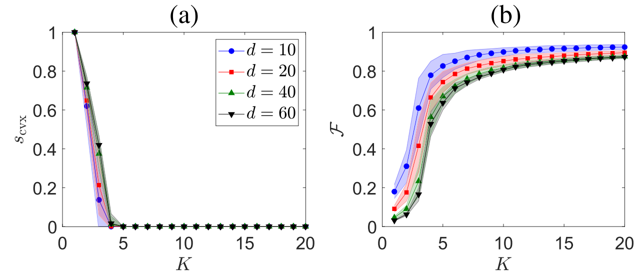

Fig. 7. RCT in high-dimensional Hilbert spaces on $|{\rm HG}_0\rangle\langle{\rm HG}_0|$ using experimental data for calibrative purposes.

For illustration, we focus on ten-dimensional states supported by 10 pre-chosen frequency bins $\{|\omega_n\rangle\langle\omega_n|\}_{n=0}^{9}$. We generate four rank-one states $\rho=|\psi\rangle\langle\psi|$ that are superpositions of such bins, namely,

$$|\psi\rangle=\frac{1}{\sqrt{3}}\begin{cases}|\omega_0\rangle+|\omega_3\rangle+|\omega_6\rangle\\ |\omega_0\rangle-|\omega_3\rangle+|\omega_6\rangle\\ |\omega_3\rangle-|\omega_6\rangle+|\omega_0\rangle\\ |\omega_6\rangle-|\omega_0\rangle+|\omega_3\rangle\end{cases}. \tag{20}$$

For mixed states of higher ranks, we consider statistical mixtures of the above four superpositions with random mixture probabilities. The measurements used to probe all these states are again random bases generated by unitary operators sampled uniformly from the Haar measure.

Figure 8 gives the performances of RCT on the class of frequency-bin states. The general behavior of $s_{\rm CVX}$ as a function of the number of bases measured K is consistent with that for the time-frequency states, confirming the basic understanding that compressive methods are system independent. The $K_{\rm IC}$ values for $r>1$ are on average larger than the those in Fig. 4, owing to more significant experimental noise present in these states, as commensurately reflected in the fidelity graphs of Fig. 8(b). The matrix

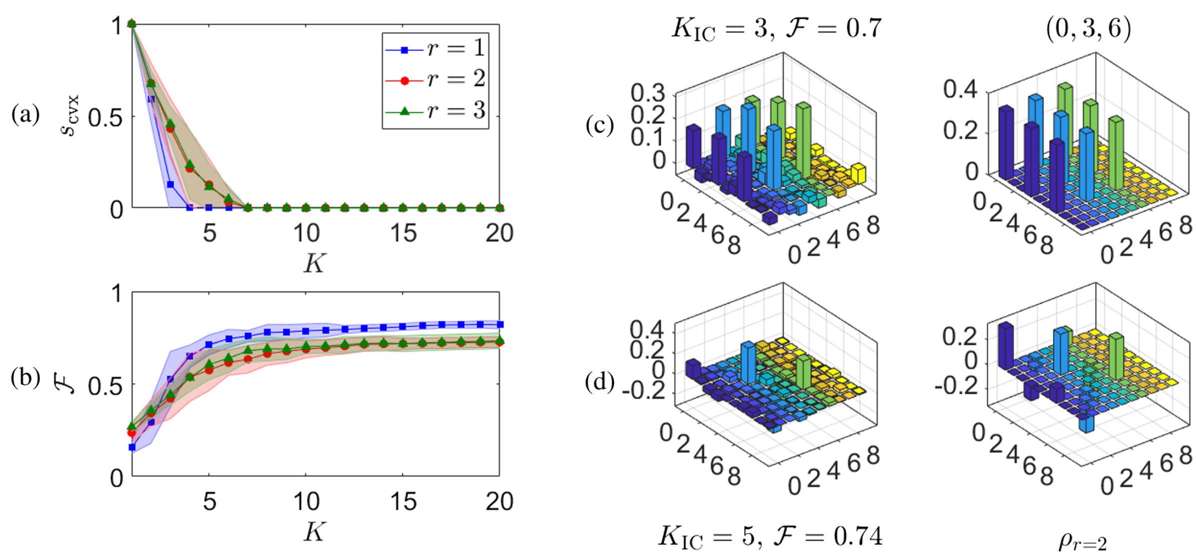

Fig. 8. Reconstruction results for frequency-bin states of $d=10$ with respect to the number of bases measured (K). The technical specifications are the same as in Fig. 4, except that for $r>1$, each run is conducted with a state that is a randomized mixture of the first r components in Eq. (20) in the stated order. (a) and (b) The behaviors of $s_{\rm CVX}$ and $\mathcal{F}$ for each rank of ρ or $\tilde{\boldsymbol{u}}$ follow similarly to those in Fig. 4. (c) and (d) Sample matrix plots of ${\rm Re}(\tilde{\boldsymbol{u}})$ for a rank-one frequency-bin superposition ($\rho=|\psi\rangle\langle\psi|$ with $|\psi\rangle=|\omega_0\rangle+|\omega_3\rangle+|\omega_6\rangle/\sqrt{3}$) and a random rank-two mixture of frequency bins (described by a $\tilde{\boldsymbol{u}}$ with eigenvalues 0.73 and 0.27) are shown.

plots of Re$\{\tilde{u}\}$ that represents all frequency-bin states present example reconstructions one would expect in typical experiments. Theoretical values of the average $K_{\rm IC}$ quoted in Section 5.B may be used as comparisons with the experimental ones.

In terms of experimental fidelity values, those for the frequency-bin state reconstructions are generally lower than those for the time-frequency state reconstructions. We note that this is not an indication of failure of the RCT scheme; the self-consistent ICC routine presented in Appendix A implies that RCT works *even for full-rank states*, albeit with a much larger $K_{\rm IC}$. Rather, we found that a higher systematic noise level is present in the frequency-bin basis measurements as compared to time-frequency basis measurements. To demonstrate that this is a major factor in influencing the optical tomography performance, we further modeled the systematic errors in the manner presented in Appendix B and showed that, indeed, such systematic errors result in lower reconstruction fidelity values.

6. CONCLUSIONS

We have demonstrated a versatile compressive quantum tomography scheme that can characterize arbitrary near-coherent quantum states in the TF domain using extremely few measurements. The method is very robust and requires no spurious assumptions about the states: this includes the degree of sparsity or coherence, which could most likely be inconsistent with the actual implementation.

From a technical perspective, our method allows for the efficient characterization of the temporal behaviour of telecommunication light at the single-photon level and can thus pave the way for many new quantum technologies.

The great performance of the method largely relies on the flexibility of the QPG, which has allowed us to implement linear optics single-photon quantum operations in terms of the temporal modes: the natural variables to deal with these signals in the quantum domain. These modes are compatible with waveguide technology, making them ideal candidates for integration into existing communication networks. In addition, they are not affected by typical medium distortions such as linear dispersion, which renders them robust basis states for real-world applications [1].

Through real experimental demonstrations, we showed that our compressive scheme can perform complete reconstruction of any TF quantum state using readily accessible algorithms that are much more versatile than the tool kits offered by conventional coherent spectroscopy.

APPENDIX A: INFORMATIONAL COMPLETENESS CERTIFICATION

Whenever a given set of bases $\mathcal{B}_L$ is *not* IC, then by definition there shall be (infinitely) many states corresponding to the physical ML probabilities $\hat{\boldsymbol{p}}_L$ extracted from the relative frequencies $\boldsymbol{\nu}_L$ of $\mathcal{B}_L$. More precisely, there exists a convex set $\mathcal{C}_L$ of states $\{\rho'\}$ that is consistent with the constraints $\rho' \geq 0$, $\mathrm{tr}\{\rho'\} = 1$, and $\langle b_{kl}|\rho'|b_{kl}\rangle = \hat{p}_{kl}$ for all $1 \leq k \leq L$ and $0 \leq l \leq d-1$.

As L increases to $L = K_{\rm IC}$, the convex set $\mathcal{C}_L \to \mathcal{C}_{K_{\rm IC}}$ eventually becomes a single point containing a unique estimator that is close to the unknown state provided that the number of photodetector clicks N for each basis measurement is sufficiently large. The task of ICC is to determine the value of $K_{\rm IC}$ at which this happens. For this purpose, we note that since $\mathcal{C}_L$ is convex, if both the minimum and maximum values over $\mathcal{C}_L$ of a *strictly convex* or *strictly concave* function of ρ' are equal to each other, then it must be the case that $\mathcal{C}_L$ is a single point of size 0. This argument clearly applies also to any linear function of ρ'.

This implies that a successful ICC involves the solution to the following equivalently semidefinite programs [68]:

ICC
Maximize and minimize $f_Z(\rho') = \mathrm{tr}\{\rho' Z\}$
subject to

- $\rho' \geq 0$,
- $\mathrm{tr}\{\rho'\} = 1$,
- $\langle b_{kl}|\rho'|b_{kl}\rangle = \hat{p}_{kl}$.

Define $s_{\rm CVX} = f_Z^{\max} - f_Z^{\min}$ and check if $s_{\rm CVX} = 0$.

Here, Z is some fixed full-rank operator that is randomly chosen. This is necessary to ensure that f_Z has no plateau structure that would violate the strict-convexity requirement. After obtaining the minimum $f_Z^{\min}$ and maximum $f_Z^{\max}$ values of f_Z, we may define $s_{\rm CVX} = f_Z^{\max} - f_Z^{\min}$. Because of the convexity properties of the entire problem of ICC, $s_{\rm CVX}$ turns out to be a monotonic indicator of the size of $\mathcal{C}_L$. If $s_{\rm CVX} = 0$, then $\mathcal{C}_L$ is a single point with $L \equiv K_{\rm IC}$. In general, an analytical understanding of the behavior of $s_{\rm CVX}$ with the number of measured bases k is apparently intangible. As an alternative, we present a numerical exposition Section 5 for the spectral-temporal optical states of interest.

APPENDIX B: SIMULATIONS FOR MODELING EXPERIMENTAL SITUATIONS

For the actual experiments, bases measurements of the different types of time-frequency modes experience varying degrees of systematic errors. The frequency-bin bases, in particular, are susceptible to a larger systematic fluctuation in their collected data than the generalized time-frequency counterparts. The small frequency span contained in a frequency bin makes it more sensitive to slight changes in the overall envelope of the pulse from which each bin is carved. These changes are related to temperature instabilities on the laboratory environment, drifts of the laser system, and small changes in the free-space optical components, among other confounding factors. This is the reason why the fidelity values for frequency-bin states are generally lower than those for time-frequency states.

To model such a situation, we introduce an effective systematic noise level $\eta_{\rm S} > 0$ that perturbs the true basis probabilities $p_{kl} = \langle b_{kl}|\rho|b_{kl}\rangle$ defined by the true state ρ. Given the true probability column $\boldsymbol{p}_k$ for the kth basis, the corresponding noisy probability column $\tilde{\boldsymbol{p}}_k = \mathcal{N}[\boldsymbol{p}_k + \eta_{\rm S}\boldsymbol{r}_k]$ is used to generate noisy relative frequencies $\tilde{\boldsymbol{\nu}}_k$, where $\mathcal{N}$ symbolizes the normalization to unit sum and $\boldsymbol{r}_k$ is a column of random numbers uniformly distributed between 0 and 1. Note that, in our case, the common practice of modeling with Gaussian $\boldsymbol{r}_k$'s typically generates too much noise that strongly deviates the $s_{\rm CVX}$ values from those observed experimentally.

Figure 9 presents the essence of the physical situation in the laboratory. The respective values of η_S used to generate the graphs for time-frequency and frequency-bin states are 0.025 and 0.05. The respective number of copies N per basis for these two kinds of states are taken to be 8,000 and 13,000, which are the typical values measured in our experiments.

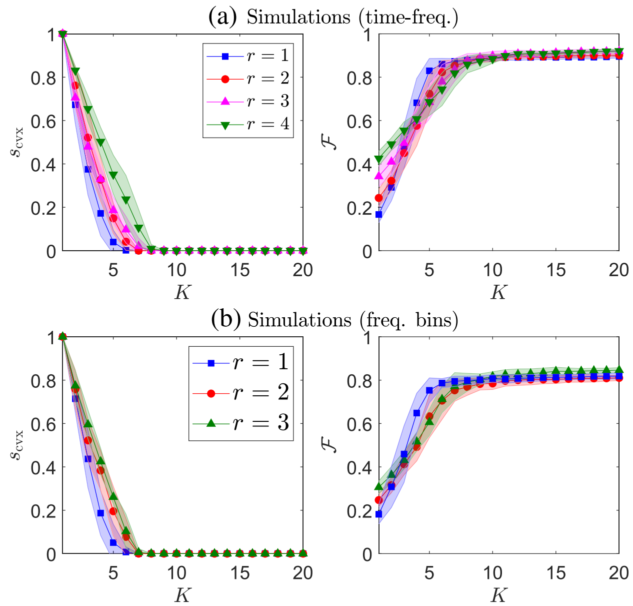

Fig. 9. Simulation results that approximately reproduce the experimental ones.

Funding. Horizon 2020 Framework Programme (ApresSF, Stormytune); Deutsche Forschungsgemeinschaft (SFB TRR 142); National Research Foundation of Korea (2019M3E4A1080074, 2019R1A6A1A10073437, 2020K2A9A1A0610294, 2020R1A2C1008609); Institute of Information & Communications Technology Planning & Evaluation (2021-0-01059, 2021-2020-0-01606); Ministerio de Ciencia e Innovación (PGC2018-099183-B-I00).

Disclosures. The authors declare no conflicts of interest.

Data Availability. All data generated or analyzed during this study are included in this published paper.

REFERENCES

1. B. Brecht, D. V. Reddy, C. Silberhorn, and M. G. Raymer, "Photon temporal modes: a complete framework for quantum information science," Phys. Rev. X **5**, 041017 (2015).
2. G. Harder, V. Ansari, T. J. Bartley, B. Brecht, and C. Silberhorn, "Harnessing temporal modes for multi-photon quantum information processing based on integrated optics," Philos. Trans. R. Soc. A **375**, 20160244 (2017).
3. S. Slussarenko and G. J. Pryde, "Photonic quantum information processing: a concise review," Appl. Phys. Rev. **6**, 041303 (2019).
4. N. Gisin and R. Thew, "Quantum communication," Nat. Photonics **1**, 165–171 (2007).
5. J. L. O'Brien, A. Furusawa, and J. Vuckovic, "Photonic quantum technologies," Nat. Photonics **3**, 687–695 (2009).
6. S. Pirandola, B. R. Bardhan, T. Gehring, C. Weedbrook, and S. Lloyd, "Advances in photonic quantum sensing," Nat. Photonics **12**, 724–733 (2018).
7. D. L. Zhou, B. Zeng, Z. Xu, and C. P. Sun, "Quantum computation based on d-level cluster state," Phys. Rev. A **68**, 062303 (2003).
8. B. P. Lanyon, M. Barbieri, M. P. Almeida, T. Jennewein, T. C. Ralph, K. J. Resch, G. J. Pryde, J. L. O'Brien, A. Gilchrist, and A. G. White, "Simplifying quantum logic using higher-dimensional Hilbert spaces," Nat. Phys. **5**, 134–140 (2009).
9. A. Babazadeh, M. Erhard, F. Wang, M. Malik, R. Nouroozi, M. Krenn, and A. Zeilinger, "High-dimensional single-photon quantum gates: concepts and experiments," Phys. Rev. Lett. **119**, 180510 (2017).
10. C. Silberhorn, V. Ansari, M. Allgaier, B. Brecht, C. Eigner, G. Harder, R. Ricken, L. Sansoni, and V. Quiring, "Quantum communication with temporal modes of pulsed light," in *Conference on Lasers and Electro-Optics (CLEO)* (2017), pp. 1–4.
11. D. Cozzolino, B. Da Lio, D. Bacco, and L. K. Oxenløwe, "High-dimensional quantum communication: benefits, progress, and future challenges," Adv. Quantum Technol. **2**, 1900038 (2019).
12. J. Yin, Y.-H. Li, S.-K. Liao, M. Yang, Y. Cao, L. Zhang, J.-G. Ren, W.-Q. Cai, W.-Y. Liu, S.-L. Li, R. Shu, Y.-M. Huang, L. Deng, L. Li, Q. Zhang, N.-L. Liu, Y.-A. Chen, C.-Y. Lu, X.-B. Wang, F. Xu, J.-Y. Wang, C.-Z. Peng, A. K. Ekert, and J.-W. Pan, "Entanglement-based secure quantum cryptography over 1,120 kilometres," Nature **582**, 501–505 (2020).
13. M. G. Raymer and I. A. Walmsley, "Temporal modes in quantum optics: then and now," Phys. Scr. **95**, 064002 (2020).
14. E. J. Candès and T. Tao, "Near-optimal signal recovery from random projections: Universal encoding strategies?" IEEE Trans. Inf. Theory **52**, 5406 (2006).
15. D. Ahn, Y. S. Teo, H. Jeong, F. Bouchard, F. Hufnagel, E. Karimi, D. Koutný, J. Řeháček, Z. Hradil, G. Leuchs, and L. L. Sánchez-Soto, "Adaptive compressive tomography with no a priori information," Phys. Rev. Lett. **122**, 100404 (2019).
16. D. Ahn, Y. S. Teo, H. Jeong, D. Koutný, J. Řeháček, Z. Hradil, G. Leuchs, and L. L. Sánchez-Soto, "Adaptive compressive tomography: a numerical study," Phys. Rev. A **100**, 012346 (2019).
17. Y. Kim, Y. S. Teo, D. Ahn, D.-G. Im, Y.-W. Cho, G. Leuchs, L. L. Sánchez-Soto, H. Jeong, and Y.-H. Kim, "Universal compressive characterization of quantum dynamics," Phys. Rev. Lett. **124**, 210401 (2020).
18. Y. S. Teo, G. I. Struchalin, E. V. Kovlakov, D. Ahn, H. Jeong, S. S. Straupe, S. P. Kulik, G. Leuchs, and L. L. Sánchez-Soto, "Objective compressive quantum process tomography," Phys. Rev. A **101**, 022334 (2020).
19. I. Gianani, Y. Teo, V. Cimini, H. Jeong, G. Leuchs, M. Barbieri, and L. Sánchez-Soto, "Compressively certifying quantum measurements," PRX Quantum **1**, 020307 (2020).
20. A. Davis, V. Thiel, M. Karpiński, and B. Smith, "Experimental single-photon pulse characterization by electro-optic shearing interferometry," Phys. Rev. A **98**, 023840 (2018).
21. C. Polycarpou, K. N. Cassemiro, G. Venturi, A. Zavatta, and M. Bellini, "Adaptive detection of arbitrarily shaped ultrashort quantum light states," Phys. Rev. Lett. **109**, 053602 (2012).
22. Z. Qin, A. S. Prasad, T. Brannan, A. MacRae, A. Lezama, and A. I. Lvovsky, "Complete temporal characterization of a single photon," Light Sci. Appl. **4**, e298 (2015).
23. W. Wasilewski, P. Kolenderski, and R. Frankowski, "Spectral density matrix of a single photon measured," Phys. Rev. Lett. **99**, 123601 (2007).
24. A. Eckstein, B. Brecht, and C. Silberhorn, "A quantum pulse gate based on spectrally engineered sum frequency generation," Opt. Express **19**, 13770–13778 (2011).
25. B. Brecht, A. Eckstein, and C. Silberhorn, "Quantum pulse gate based on ultrafast frequency upconversion," in *Conference on Lasers and Electro-Optics Europe and 12th European Quantum Electronics Conference (CLEO EUROPE/EQEC)* (2011), pp. 1.
26. B. Brecht, A. Eckstein, A. Christ, H. Suche, and C. Silberhorn, "From quantum pulse gate to quantum pulse shaper engineered frequency conversion in nonlinear optical waveguides," New J. Phys. **13**, 065029 (2011).
27. V. Ansari, G. Harder, M. Allgaier, B. Brecht, and C. Silberhorn, "Temporal-mode measurement tomography of a quantum pulse gate," Phys. Rev. A **96**, 063817 (2017).
28. C. Iaconis, E. Mukamel, and I. A. Walmsley, "Temporal heterodyne detector for multitemporal mode quantum state measurement," J. Opt. B **2**, 510–516 (2000).
29. O. Morin, C. Fabre, and J. Laurat, "Experimentally accessing the optimal temporal mode of traveling quantum light states," Phys. Rev. Lett. **111**, 213602 (2013).
30. J. M. Lukens and P. Lougovski, "Frequency-encoded photonic qubits for scalable quantum information processing," Optica **4**, 8–16 (2017).
31. D. Rieländer, A. Lenhard, O. J. Faras, A. Máttar, D. Cavalcanti, M. Mazzera, A. Acn, and H. de Riedmatten, "Frequency-bin entanglement of ultra-narrow band non-degenerate photon pairs," Quantum Sci. Technol. **3**, 014007 (2017).
32. H.-H. Lu, J. M. Lukens, N. A. Peters, B. P. Williams, A. M. Weiner, and P. Lougovski, "Quantum interference and correlation control of frequency-bin qubits," Optica **5**, 1455–1460 (2018).
33. J. M. Lukens, "Quantum information processing with frequency-bin qubits: progress, status, and challenges," in *Conference on Lasers and Electro-Optics (CLEO)* (2019), pp. 1–2.

34. H.-H. Lu, J. M. Lukens, B. P. Williams, P. Imany, N. A. Peters, A. M. Weiner, and P. Lougovski, "A controlled-NOT gate for frequency-bin qubits," npj Quantum Inf. **5**, 24 (2019).
35. I. N. Chuprina and A. A. Kalachev, "Generating frequency-bin qubits via spontaneous four-wave mixing in a photonic molecule," Phys. Rev. A **100**, 043843 (2019).
36. H.-H. Lu, E. M. Simmerman, P. Lougovski, A. M. Weiner, and J. M. Lukens, "Fully arbitrary control of frequency-bin qubits," Phys. Rev. Lett. **125**, 120503 (2020).
37. C. Fabre and N. Treps, "Modes and states in quantum optics," Rev. Mod. Phys. **92**, 035005 (2020).
38. J. Paye, "The chronocyclic representation of ultrashort light pulses," IEEE J. Quantum Electron. **28**, 2262–2273 (1992).
39. M. Beck, M. G. Raymer, I. A. Walmsley, and V. Wong, "Chronocyclic tomography for measuring the amplitude and phase structure of optical pulses," Opt. Lett. **18**, 2041–2043 (1993).
40. L. Praxmeyer and K. Wódkiewicz, "Time and frequency description of optical pulses," Laser Phys. **15**, 1477 (2005).
41. I. A. Walmsley and C. Dorrer, "Characterization of ultrashort electromagnetic pulses," Adv. Opt. Photon. **1**, 308–437 (2009).
42. B. Brecht and C. Silberhorn, "Characterizing entanglement in pulsed parametric down-conversion using chronocyclic Wigner functions," Phys. Rev. A **87**, 053810 (2013).
43. E. P. Wigner, "On the quantum correction for thermodynamic equilibrium," Phys. Rev. **40**, 749–759 (1932).
44. V. Ansari, J. M. Donohue, B. Brecht, and C. Silberhorn, "Remotely projecting states of photonic temporal modes," Opt. Express **28**, 28295–28305 (2020).
45. G. Patera, D. B. Horoshko, J. Shi, and M. I. Kolobov, "Quantum temporal imaging with squeezed light," Proc. SPIE **10674**, 106740E (2018).
46. V. Ansari, E. Roccia, M. Santandrea, M. Doostdar, C. Eigner, L. Padberg, I. Gianani, M. Sbroscia, J. M. Donohue, L. Mancino, M. Barbieri, and C. Silberhorn, "Heralded generation of high-purity ultrashort single photons in programmable temporal shapes," Opt. Express **26**, 2764–2774 (2018).
47. V. Ansari, J. M. Donohue, M. Allgaier, L. Sansoni, B. Brecht, J. Roslund, N. Treps, G. Harder, and C. Silberhorn, "Tomography and purification of the temporal-mode structure of quantum light," Phys. Rev. Lett. **120**, 213601 (2018).
48. M. A. Cox, L. Maqondo, R. Kara, G. Milione, L. Cheng, and A. Forbes, "The resilience of Hermite– and Laguerre–Gaussian modes in turbulence," J. Lightwave Technol. **37**, 3911–3917 (2019).
49. Y. S. Teo, B. Stoklasa, B.-G. Englert, J. Řeháček, and Z. Hradil, "Incomplete quantum state estimation: a comprehensive study," Phys. Rev. A **85**, 042317 (2012).
50. Y. S. Teo, *Introduction to Quantum-State Estimation* (World Scientific, 2015).
51. V. Ansari, J. M. Donohue, B. Brecht, and C. Silberhorn, "Tailoring nonlinear processes for quantum optics with pulsed temporal-mode encodings," Optica **5**, 534–550 (2018).
52. W. Pauli, *Die allgemeinen Prinzipen der Wellenmechanik, Handbuch der Physik* (Springer, 1933), Vol. **24**.
53. A. Peres, *Quantum Theory: Concepts and Methods* (Kluwer, 1993).
54. J. Aldrich, "R. A. Fisher and the making of maximum likelihood 1912–1922," Stat. Sci. **12**, 162–176 (1997).
55. K. Banaszek, "Maximum-likelihood algorithm for quantum tomography," Acta Phys. Slov. **49**, 633–638 (1999).
56. J. Řeháček, Z. Hradil, E. Knill, and A. I. Lvovsky, "Diluted maximum-likelihood algorithm for quantum tomography," Phys. Rev. A **75**, 042108 (2007).
57. Y. S. Teo, H. Zhu, B.-G. Englert, J. Řeháček, and Z. Hradil, "Quantum-state reconstruction by maximizing likelihood and entropy," Phys. Rev. Lett. **107**, 020404 (2011).
58. J. Shang, Z. Zhang, and H. K. Ng, "Superfast maximum-likelihood reconstruction for quantum tomography," Phys. Rev. A **95**, 062336 (2017).
59. J. Shang, Z. Zhang, and H. K. Ng, "Efficient MATLAB routines for quantum tomography," Github (2017), https://github.com/qMLE/qMLE, (The codes that are used to generate the results in this article are downloadable here.)
60. M. Silver, Y.-P. Huang, C. Langrock, M. M. Fejer, P. Kumar, and G. S. Kanter, "Three-signal temporal-mode selective upconversion demultiplexing," IEEE Photon. J. **31**, 1749–1752 (2019).
61. J. Gil-Lopez, M. Santandrea, B. Brecht, G. Roland, R. Ricken, V. Quiring, and C. Silberhorn, "Improved non-linear devices for quantum applications," New J. Phys. **23**, 063082 (2021).
62. G. M. Gibson, S. D. Johnson, and M. J. Padgett, "Single-pixel imaging 12 years on: a review," Opt. Express **28**, 28190–28208 (2020).
63. N. Tomm, A. Javadi, N. O. Antoniadis, D. Najer, M. C. Löbl, A. R. Korsch, R. Schott, S. R. Valentin, A. D. Wieck, A. Ludwig, and R. J. Warburton, "A bright and fast source of coherent single photons," Nat. Nanotechnol. **16**, 399–403 (2021).
64. M. Allgaier, G. Vigh, V. Ansari, C. Eigner, V. Quiring, R. Ricken, B. Brecht, and C. Silberhorn, "Fast time-domain measurements on telecom single photons," Quantum Sci. Technol. **2**, 034012 (2017).
65. C. K. Law, I. A. Walmsley, and J. H. Eberly, "Continuous frequency entanglement: effective finite Hilbert space and entropy control," Phys. Rev. Lett. **84**, 5304–5307 (2000).
66. F. Mezzadri, "How to generate random matrices from the classical compact groups," Not. Am. Math. Soc. **54**, 592–604 (2007).
67. K. Życzkowski, K. A. Penson, I. Nechita, and B. Collins, "Generating random density matrices," J. Math. Phys. **52**, 062201 (2011).
68. L. Vandenberghe and S. Boyd, "Semidefinite programming," SIAM Rev. **38**, 49–95 (1996).